



Contents lists available at ScienceDirect

Arabian Journal of Chemistry

journal homepage: www.ksu.edu.sa

Original article



Development of *in vitro* and *in vivo* c-Met targeted dual-modal nanoprobe for NIR II fluorescent bioimaging and magnetic resonance imaging of breast carcinoma metastasis

Jingbo Wang^{a,1}, Lin Yang^{a,b,1}, Weilong Ding^{a,1}, Weiqing Tang^{a,*}, Ying Yuan^{a,*}, Xiaofeng Tao^{a,*}

^a Shanghai Ninth People's Hospital, Shanghai Jiao Tong University, Shanghai 200011, China

^b Fujian branch of Shanghai children's medical center, Fujian children's hospital, China

ARTICLE INFO

Keywords:

c-Met binding polypeptides (cMBP)
TNBC diagnosis
Fe₃O₄
NIR II fluorescent imaging
MRI

ABSTRACT

Because of the conventional bioimaging methods, including ultrasound and X-ray examinations often lack accuracy and sensitivity in the early diagnosis, as a heterogeneous subtype of breast cancer, it remains an urgent need to develop efficaciously and sensitively diagnostic drivers of triple negative breast cancer (TNBC). The overexpression of c-mesenchymal epithelial transition-factor (c-Met) is associated with the basal subtype of breast carcinoma and linked with decreased survival rate of TNBC patients. Here, we have synthesized a dual-modal nanoprobe with luminescence imaging in the bio-window of near infrared II region (NIR II, 1000–1700) and magnetic resonance imaging (MRI) performances. After c-Met targeting binding protein decoration, this Fe₃O₄@mSiO₂-ICG/cMBP had outstanding size stability and preminent biocompatibility. Meaningfully, it presented effective TNBC cells recognition *in vitro*. Besides, after caudal-vein injection of this nanoprobe, both NIR II luminescence imaging and MRI demonstrated that it can more efficiently concentrated in metastatic TNBC tumors in comparison with Fe₃O₄@mSiO₂-ICG and clinical used Gd-DTPA. Meanwhile, the core-shell nanoprobe also showed negligible toxicity *in vivo*. All results suggested that our cMBP modified nanocomposite could provide a fascinating and efficient non-invasive diagnostic tool for TNBC detection in clinic.

1. Introduction

As the 2nd cause of tumor associated death, breast diagnosis plays a vital role in reducing the excessive cancer mortality among women (Corti, et al., 2021; Lugert, et al., 2018; Siegel, et al., 2022; Takahashi, et al., 2013) Further, breast cancers are primarily subjected to surgical resection with adequate negative margins to guarantee through removal with minimizing functional impairment that related to the procedure (Terada, et al., 2022; Yu, et al., 2017). Once suspicious lesions in the breast cavity are visually observed, as the gold standard, biopsy-based pathological diagnosis will be conducted to discriminate whether they are malignant or benign tissues (Wu, et al., 2021). However, the initial diagnosis and the final pathological analysis after total specimen resection often could find an inconsistency, that is mainly ascribed to the tumor heterogeneity, like triple negative breast cancer (TNBC) (Asleh,

et al., 2022; Marra, et al., 2020). Accordingly, there is an urgent demand to engineer a noninvasive, safety and ultra-sensitive diagnostic strategy to detect breast carcinomas and finally improving the early diagnosis rate and raising the survival rate. Fortunately, molecular imaging has been developed as the optimal approach for the early diagnosis and followed prognostic estimation of numerous diseases (Antaris, et al., 2016; McHugh, et al., 2018; Ren, et al., 2018; Smeden, et al., 2021; Sun, et al., 2019) Besides, molecular imaging with targeted capability that mainly comprised of the tumor biomarkers (Bai, et al., 2023; Fu, et al., 2021; Zhao, et al., 2020). Specifically, the most attractive imaging biomarkers for breast cancer is the overexpressed c-mesenchymal epithelial transition-factor (c-Met) that has been regarded as a tyrosine kinase receptor (Wu, et al., 2018; Wu, et al., 2020; Xu, et al., 2011). It has been demonstrated as a novel therapeutic target motif, especially in breast carcinoma (Charafe-Jauffret, et al., 2006; Goncalves, et al., 2008;

* Corresponding authors at: Shanghai Ninth People's Hospital, Shanghai Jiao Tong University, Shanghai 200011, China.

E-mail addresses: 13817017639@163.com (W. Tang), yuan83@163.com (Y. Yuan), cjr.taofeng@vip.163.com (X. Tao).

¹ These authors contributed equally to this work and are considered co-first authors.

<https://doi.org/10.1016/j.arabjc.2024.105919>

Received 11 December 2023; Accepted 18 July 2024

Available online 28 July 2024

1878-5352/© 2024 The Author(s). Published by Elsevier B.V. on behalf of King Saud University. This is an open access article under the CC BY-NC-ND license (<http://creativecommons.org/licenses/by-nc-nd/4.0/>).

Hochgräfe, et al., 2010) However, it is still urgently needed to develop a specific targeted treatment, particularly for the most aggressive subtype, like TNBC.

PET contrast agent, ^{18}F -labeled c-Met binding polypeptides (cMBP) have been developed to specifically recognized c-Met protein on malignancy imaging (Li, et al., 2023). However, the nerves surrounding breast cancers that are vulnerable to ionizing irradiation. Owing to the excellent depth penetration, high spatial resolution and low background scattering signals of second near infrared region (NIR II, 1000–1700 nm) fluorescence imaging, it has been widely studied for breast cancer diagnosis (Wang, et al., 2022; Wei, et al., 2023; Xu, et al., 2022; Yang, et al., 2022) In the bargain, c-Met targeted rare-earth nanoplatform was designed for successful diagnosis of TNBC by NIR II fluorescence bio-imaging (Wang, et al., 2021) nevertheless, low fluorescence quantum yield of this reported c-Met lanthanide nanocrystal was also not suitable for TNBC diagnosis. Additionally, accurate and wealthy information under various tissue penetration depths or scales cannot be effectively provided through the single fluorescence imaging (He, et al., 2018; Li, et al., 2019) Interestingly, in modern clinical medicine, Magnetic resonance imaging (MRI) presents outstanding performance, especially, compared with NIR II fluorescence imaging, it offers higher spatial resolution (Lee, et al., 2016; Zheng, et al., 2021) Accordingly, considering the desirable properties of these two imaging modalities, integration of NIR II fluorescence imaging and MIR could accurately discriminate TNBC by compensating the inherent limitations of each other.

Superparamagnetic iron oxide nanoparticles and uniform Fe-based nanocrystals, such as Fe_3O_4 and Fe_2O_3 have been concerned in the reported works for decades (Dubravka, et al., 2018) Because of their numerous biomedical applications, like MRI (Barick, et al., 2014), precisely drug delivery (Wang, et al., 2022), photothermal therapy and magnetic fluid hyperthermia tumor inhibition (Chu, et al., 2013). As an important MRI contrast agent, Fe_3O_4 nanoparticles and its analogues have been intensively concerned on account of their low price and outstanding high biocompatibility (Yang, et al., 2020). Intriguingly, clinically approved indocyanine green (ICG) generates long off-peak NIR II emission spectra with biocompatibility, although the emission peak is not in the NIR II window, it still has high quantum yields in the off-peak

region, especially higher than the most of NIR-II inorganic nanoprobes (Antaris, et al., 2017; Gao, et al., 2023). The reported Fe_3O_4 nanoagents often lack a large specific surface area for carrying drug molecules. Hence, Fe-based nanocores and a perpendicularly aligned mesoporous SiO_2 shell were synthesized (Deng, et al., 2008; Fan, et al., 2019; Rajarathinam, et al., 2019). Thus, mesoporous silica shell coated Fe_3O_4 and ICG containing nanoprobes anchored with cMBP for efficient diagnosis of TNBC have not been explored.

In this research, uniformed Fe_3O_4 nanocores were coated with mesoporous silica nanoshells which was applied for ICG efficacious loading. After surface PEGylation and modification of cMBP ($\text{Fe}_3\text{O}_4@\text{mSiO}_2\text{-ICG/cMBP}$) for precise diagnosis of metastatic TNBC model in mice (Fig. 1). The data showed that this nanoprobe exhibited prominent size stability and biocompatibility. After cMBP modification, it also had excellent cellular internalization, moreover, this nanoprobe showed a higher contrast compared with the normal surrounding tissues *in vivo*. Exceptional NIR II luminescent imaging and superior MRI capability and features of the nanoprobe could recognize TNBC metastasis *in vivo* with low systemic toxicity which highlighted our work and our novel nanoprobes also provided a promising contrast agent for biomedical application of early TNBC diagnosis.

2. Materials and methods

2.1. Preparation of Fe_3O_4

The magnetic Fe_3O_4 nanocores were synthesized by the common solvo-thermal strategy (Liu, et al., 2020). Briefly, 2.7 g of $\text{FeCl}_3\cdot 6\text{H}_2\text{O}$, 7.2 g of sodium acetate were concurrently added into 100 mL ethylene glycol solution with vigorous magnetic stirring (1000 rpm/min). Above homogenous-yellow aqueous mixture was carefully transferred into a 100 mL of Teflon-lined stainless-steel autoclave which was sealed and maintained in an oven 200°C for 8 hr. Subsequently, the autoclave cooled down at room temperature and the as-made black magnetic Fe_3O_4 nanoparticles were washed by anhydrous ethanol for 10-times and the prepared Fe-based samples were dried over-night at 60°C.

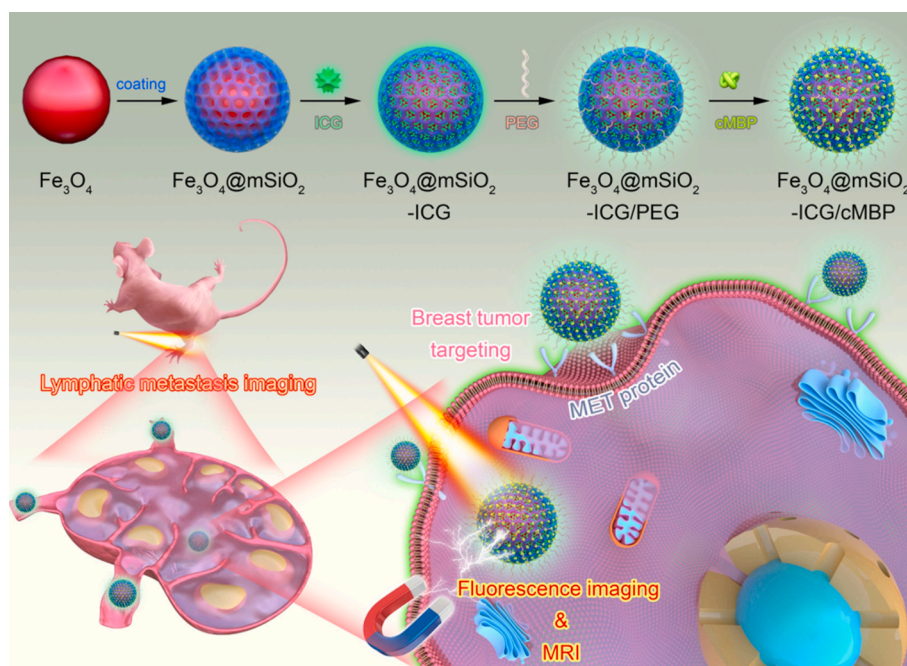


Fig. 1. Schematic illustration of the step-by-step development of $\text{Fe}_3\text{O}_4@\text{mSiO}_2\text{-ICG/cMBP}$ nanoprobes for MRI and NIR II fluorescence imaging of lymphatic TNBC metastasis.

2.2. Synthesis of Fe_3O_4 @ mSiO_2

Mesoporous silica coating was fabricated according to previous report work (Wei, et al., 2023). For silica based nanoshell wrapping, 100 mg of Fe_3O_4 nanoparticles were pre-treated with 50 mL, 0.1 mol/L of hydrochloric acid with a 10 min of continuous sonication. Then the hydrophilic magnetic nanocrystals were collected by a magnet and washed 3-times by deionized water. Thereafter, the prepared Fe-based nanoparticles were added in aqueous solution, containing 70 mL of ethanol, 80 mL of deionized water and 0.3 g of cetyltrimethyl ammonium bromide (CTAB). After vigorous magnetic stirring (450 rpm/min) for preparing a homogenous dispersion, 1.2 mL, 28 % ammonia was added and maintained stirring for 1 h. Latterly, 0.3 mL of tetraethyl orthosilicate was put into the above mixed solution and carried out a continuous magnetic stir for at 37 °C 12 hr. These core-shell magnetic nanoparticles Fe_3O_4 @ mSiO_2 with mesoporous shells were separated and washed sequentially by ethanol and deionized water for 6-times, then, the collected samples were re-dispersed in a 60 mL, 1 % NH_4NO_3 aqueous solution which was subjected to a sustained refluxing for 12 h. The final core-shell Fe_3O_4 @ mSiO_2 were obtained by a magnet, washed with anhydrous ethanol, and dried at 60 °C vacuum over-night.

2.3. PEGylation of Fe_3O_4 @ mSiO_2

Out-layer silica surface PEGylation was then performed. Typically, 50 mg of Fe_3O_4 @ mSiO_2 was added in 10 mL of aqueous solution containing 100 mg of $\text{PEG}_{2000}\text{-NH}_2$. The mixture was gently stirred for 12 hr at room temperature, the amino group's decorated Fe_3O_4 @ mSiO_2 nanocomposite (Fe_3O_4 @ mSiO_2 -PEG) were successfully prepared. Immediately, residual $\text{PEG}_{2000}\text{-NH}_2$ was removed by 3-times washing with water by a high-speed centrifugation (17000 rpm, 0.5 hr).

2.4. ICG loading in Fe_3O_4 @ mSiO_2 -PEG

Briefly, 2 mg of ICG was pre-dispersed in 6 mL of anhydrous ethanol with strong ultrasonication. Thereafter, 60 mg of the as-prepared Fe_3O_4 @ mSiO_2 -PEG nanoparticles were instantly poured to the prepared ICG-ethanol mixture. The ICG/ Fe_3O_4 @ mSiO_2 -PEG solution was continuously and intensely stirred at a 37 °C oil-bath for 48 hr. At present, NIR II contrast agent, ICG was successfully adsorbed by the mesopores in the nanoshells. The as-prepared ICG encapsulated Fe_3O_4 @ mSiO_2 -PEG nanocomposite (Fe_3O_4 @ mSiO_2 - ICG/PEG) was render 3-times of centrifugal washing (10 min, 5000 rpm) with deionized water.

2.5. cMBP modification on Fe_3O_4 @ mSiO_2 -ICG

At last, Fe_3O_4 @ mSiO_2 -ICG/cMBP was constructed using condensation reaction. (Xie, et al., 2023). Firstly, 2 mg of cMBP protein was added into 2-(N-morpholino) ethane-sulfonic acid buffer (5 mL, 0.1 mol/L, pH=5.5). Secondly, 20 mg, 25 mg of N-(3-dimethylaminopropyl)-N'-ethylcarbodiimide hydrochloride (EDC) and N-hydroxysuccinimide (NHS) were simultaneously introduced into the above cMBP based mixture. An intense and continuous stirring was performed on this mixture for 2 hr at room temperature. Thereafter, 60 mg of Fe_3O_4 @ mSiO_2 -ICG was added in the above cMBP based mixture with gent stirring for 12 hr. cMBP-decorated Fe_3O_4 @ mSiO_2 -ICG was obtained by centrifugal washing (10 min, 5000 rpm) with H_2O and the finally Fe_3O_4 @ mSiO_2 -ICG/cMBP nanoprobes were re-dispersed in H_2O and stored at 4°C.

2.6. Development of lymphatic metastasis model

All animal studies in this work were performed according to the Care and Use Guidelines for Lab Animals of Shanghai University and the procedures were also approved by the Animal-Ethics-Committee (Shanghai University). 6 weeks old, female Balb/c nude mice were

bought from SLAC Lab Animal Co., Ltd. (Shanghai, China) and they were fed adaptively for 7 days before TNBC tumor bearing. In this work, a lymphatic metastasis-bearing mouse model was successfully established by injecting 25 μL , 5×10^5 (PBS 1X) of MDA-MB 231 cells into the left-foot pad of naked mice. The metastatic model was monitored by touching and stroking the enlarged lymph nodes at each 3 days and histological-analysis on postinjection of 10 days. Successful lymphatic metastasis model can be acquired at 14 days post injection.

2.7. NIR II fluorescence bio-imaging of lymphatic metastasis

Above prepared lymphatic metastasis bearing-nude mice were firstly divided into 2 groups (n = 5). Real-time NIR II luminescence imaging procedure started at 15 min, 1 hr, 3 hr, 12 hr, 24 hr and 48 hr post tail-vein administration of 15 mg/kg Fe_3O_4 @ mSiO_2 -ICG and Fe_3O_4 @ mSiO_2 -ICG/cMBP, respectively. NIR II fluorescent bioimages were obtained via 1000-nm long-pass filter, 300-ms exposure time and 808-nm light excitation (400 mW/cm²).

2.8. MRI of lymphatic metastasis

The established lymphatic metastasis bearing-nude mice were firstly divided into 2 groups (n = 5). Real-time MRI procedure started at 15 min, 1 hr, 2 hr, 3 hr, 4 hr, 6 hr, 12 hr and 24 hr and 48 hr post tail-vein administration of 15 mg/kg Fe_3O_4 @ mSiO_2 -ICG/cMBP, respectively. Mice with tail vein injection of Gd-DTPA for 15 min, 1 hr, 2 hr, 3 hr were conducted as the control group. T1-weighted bioimages were acquired using a 3.0 T magnetic resonance (MR) scanner.

3. Results and discussion

3.1. Synthesis of Fe_3O_4 @ mSiO_2 -ICG/cMBP

Fe_3O_4 @ mSiO_2 -ICG/cMBP with superparamagnetic features were acted as the versatile carrier for accurate diagnosis of TNBC. The detailed step-by-step procedure for the preparation of this novel nanoprobe was illustrated in Fig. 1. Firstly, dispersible and hydrophilic Fe_3O_4 nanocores were fabricated by a conventional solvothermal strategy by using ethylene glycol as the redundant and solvent. $\text{FeCl}_3 \cdot 6\text{H}_2\text{O}$ was acted as the Fe source in the presence of sodium acetate. After 8 hr reaction under 200°C, the black Fe_3O_4 nanocrystals can be obtained. According to the images from transmission electron microscope (TEM) and scanning electron microscope (SEM), Fe_3O_4 nanoparticles with uniform diameter (~70 nm) can be clearly observed (Fig. 2A, D). Secondly, the as-prepared Fe_3O_4 nanocrystals were coated with mesoporous silica nanoshell, in which CTAB served as the stabilizing surfactant on Fe_3O_4 surface and soft template for the silica nanocomponent formation in the sol-gel reaction. The CTAB template in the silica nanoshell was removed by an ion-exchange of ammonium nitrate, clearly, the mesoporous shell became and accordingly, mesoporous silica coated magnetite with core-shell nanostructure (Fe_3O_4 @ mSiO_2) with size of ~200 nm could be successfully prepared (Fig. 2B, E). Meanwhile, from the dynamic laser scattering (DLS) data, the size increased from 71 nm to 195 nm after silica coating which were consisted with TEM and SEM photographs (Fig. 2G, H). Furthermore, The X-ray diffraction pattern of Fe_3O_4 @ mSiO_2 nanocomposites presented the characteristic peaks of Fe_3O_4 nanocrystals (JCPDS 9-0866), demonstrating that the composites of this Fe-based nanocrystals in core-shell nanoparticles (Fig. 2I). Besides, the mesopores observing under SEM (Fig. 2E), the porous structure of the prepared Fe_3O_4 @ mSiO_2 was appraised by a nitrogen-absorption/desorption isotherms curve. As displayed in Fig. 2J, according to the Brunauer-Emmett-Teller (BET), the specific surface area of Fe_3O_4 @ mSiO_2 was determined as ~254 m²/g. The pore distributions of silica shell showed a clear unequal mesopore diameter of 8.8 nm (Fig. 2K). These data demonstrated that the core-shell nanocomposite can be further used for drug delivery nanoplatfrom (Rajarithnam, et al.,

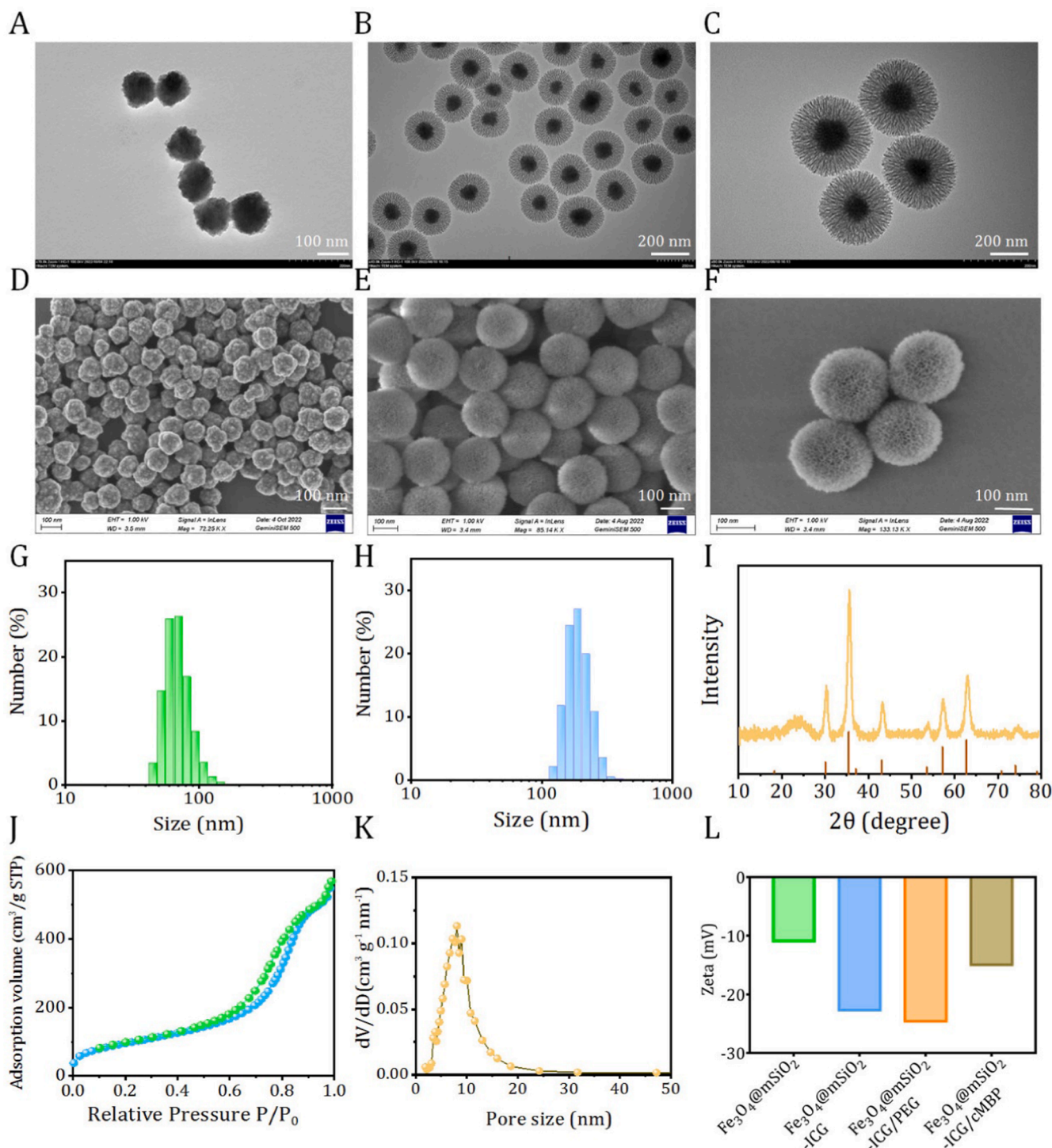


Fig. 2. TEM images of Fe₃O₄ (A), Fe₃O₄@mSiO₂ (B) and Fe₃O₄@mSiO₂-ICG/cMBP (C). SEM images of Fe₃O₄ (D), Fe₃O₄@mSiO₂ (E) and Fe₃O₄@mSiO₂-ICG/cMBP (F).

2024; Rajarathinam, et al., 2021; Jayaraman, et al., 2023). It has been extensively demonstrated that ICG possessed high shortwave infrared fluorescence imaging quality in the off-peak emission tail (beyond 1000 nm) (Carr, et al., 2018; Hu, et al., 2020), in this work, we firstly evaluated the NIR II imaging feature of ICG solution with a 1000 nm long-pass filter (LP1000). Clearly, the increase in NIR II signal was concentration dependent (Fig. S1). Thirdly, ICG dyes were absorbed in the mesoporous shell (Fe₃O₄@mSiO₂-ICG), and then PEG₂₀₀₀-NH₂ was grafted on the surface for the subsequent cMBP conjugation (Fe₃O₄@mSiO₂-ICG)/PEG). Finally, the targeting motifs were anchored

on the out-layer of silica by a common condensation reaction (Fe₃O₄@mSiO₂-ICG/cMBP). The core-shell nanoprobes still maintained the core-shell morphology and mesoporous structure after ICG loading and cMBP grafting (Fig. 2C, F). Owing to the negative charges of ICG and PEG₂₀₀₀-NH₂, after ICG encapsulation and PEGylation, zeta potential decreased which could be ascribed to the consumption of -NH₂ groups (Fig. 2L). Negative surface charge can reduce nanobio interactions, facilitating anionic nanoprobes to migrate from micro-vessels within the extracellular space and extensively distribute throughout the tumor tissue

(Souri, et al., 2024). Besides, $\text{Fe}_3\text{O}_4@\text{mSiO}_2\text{-ICG/cMBP}$ is then studied by Fourier-transform infrared spectrometer (FTIR), distinctly, a strengthened peak locating at 3300 cm^{-1} must be assigned to the new generate amide bond and two emerged peaks at 1229 cm^{-1} , 1090 cm^{-1} were originated from amino acids in cMBP (Fig. S2). Slight size variation can be visualized in $\text{Fe}_3\text{O}_4@\text{mSiO}_2\text{-ICG/cMBP}$ and its diameter finally increases from 195 nm to $\sim 220\text{ nm}$ (Fig. S3), profoundly indicating the outlayer PEGylating and cMBP grafting. The results primarily indicated the successful development of $\text{Fe}_3\text{O}_4@\text{mSiO}_2\text{-ICG/cMBP}$.

DLS results of Fe_3O_4 (G) and $\text{Fe}_3\text{O}_4@\text{mSiO}_2$ (H). XRD patterns of Fe_3O_4 and $\text{Fe}_3\text{O}_4@\text{mSiO}_2$ (I). The N_2 absorption/desorption plot of $\text{Fe}_3\text{O}_4@\text{mSiO}_2$ (J). Pore size distribution of $\text{Fe}_3\text{O}_4@\text{mSiO}_2$ (K). Zeta potential data of $\text{Fe}_3\text{O}_4@\text{mSiO}_2$ based nanoplatforms (L).

3.2. Characterization of $\text{Fe}_3\text{O}_4@\text{mSiO}_2\text{-ICG/cMBP}$

Recently, mesoporous silica nanoparticles (mSiO_2) are increasingly put forward as promising candidate for drug delivery nanocarriers and thus prominently improving the saturation solubility of poorly dissolve nanocompounds (Ibrahim, et al., 2020). We then fabricated the mSiO_2 nanocarriers with the same size of Fe-based core-shell nanoplatform (Fig. S4, S5). In the meantime, these silica nanospheres also had similar specific area and pore size (Fig. S6). Compared with ICG loaded and cMBP anchored mSiO_2 ($\text{mSiO}_2\text{-ICG/cMBP}$) that dispersed in pure water to a variety of dosage, no apparent sediments or flocs were found in

$\text{Fe}_3\text{O}_4@\text{mSiO}_2$ and $\text{Fe}_3\text{O}_4@\text{mSiO}_2\text{-ICG/cMBP}$ groups, even if the concentration reaches up to $1500\text{ }\mu\text{g/mL}$ (Fig. 3A-C). These results demonstrated that our nanoprobos of Fe_3O_4 nanocrystals with porous outer shells, ICG loading and targeting motif binding had an excellent aqueous dispersion behavior. Understanding the nanoparticles size variations in various physiological media plays a vital role in determining the following bio-application fate, we then investigated the size stability of our nanoprobos toward different biological buffers. As depicted in Fig. 3D-E, obviously, no evident size fluctuations of $\text{mSiO}_2\text{-ICG/cMBP}$, $\text{Fe}_3\text{O}_4@\text{mSiO}_2$ and $\text{Fe}_3\text{O}_4@\text{mSiO}_2\text{-ICG/cMBP}$ were monitored even after 48 h immersion in 0.9 % NaCl, PBS, and cell medium, respectively, confirming the stable size feature of this nanoprobos. Furthermore, the hemolytic properties of our synthetic Fe-based nanoparticles were conducted. The hemolysis rate of $\text{Fe}_3\text{O}_4@\text{mSiO}_2\text{-ICG/cMBP}$ slightly increased 3.8 % to 12 % when the concentration of these nanoprobos were set from $500\text{ }\mu\text{g/mL}$ to $1500\text{ }\mu\text{g/mL}$, and no significant discrepancy were discovered among the three nanoplatforms (Fig. 3G, S7), laying the solid foundation for subsequent *in vivo* research. Additionally, the c-Met binding affinity was subsequently studied, FITC labelled $\text{Fe}_3\text{O}_4@\text{mSiO}_2$ with cMBP modification ($\text{Fe}_3\text{O}_4@\text{mSiO}_2\text{-FITC/cMBP}$) was prepared in advance, then it was immersed in c-Met enveloped microtiter plate in a dose-dependent way. The absorbance data showed that cMBP modified nanoprobos gradually increased with the incubation time. According to the reported works, cMBP could specifically bind with c-Met against hepatocyte growth factor (HGF) (Wu

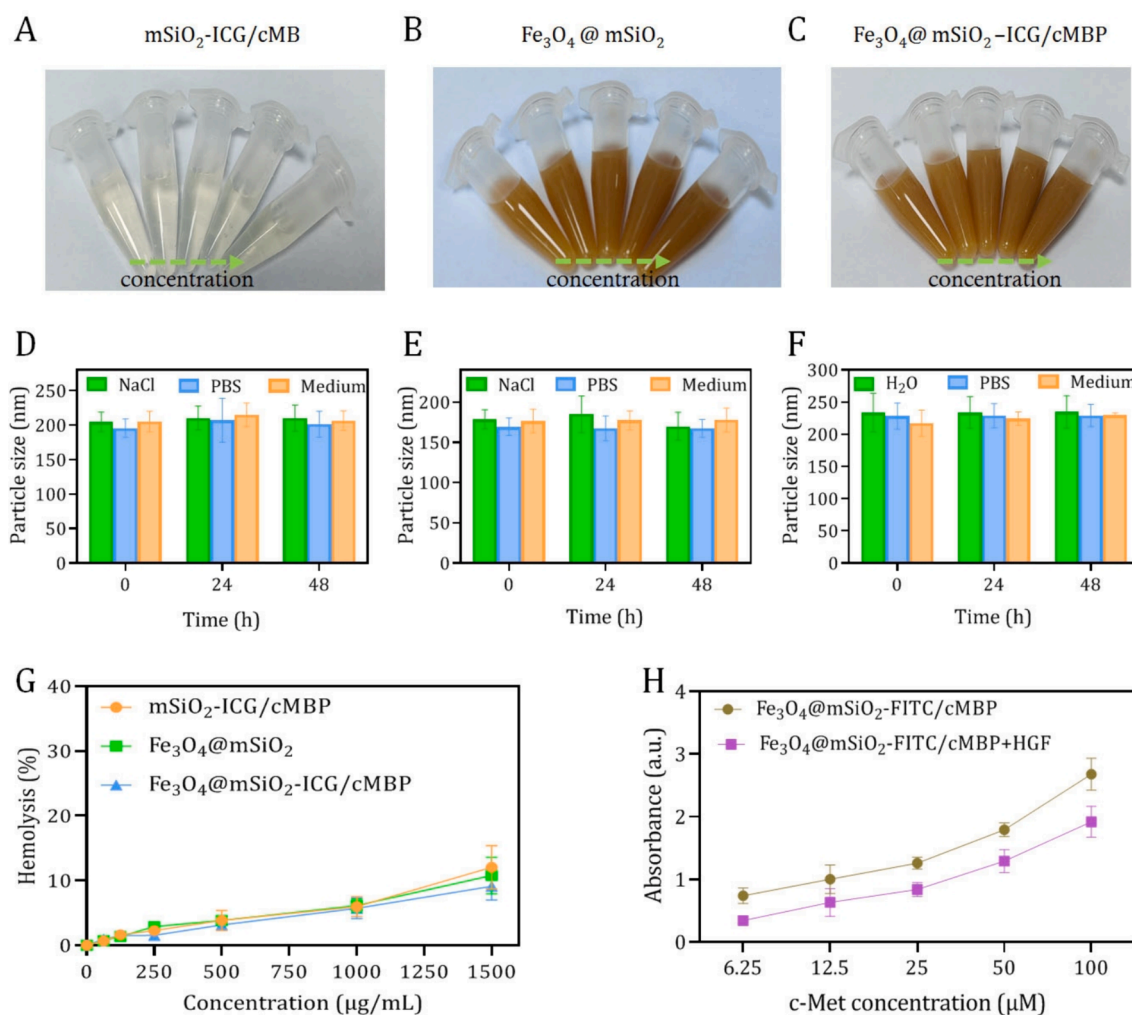


Fig. 3. Representative digital photos of $\text{mSiO}_2\text{-ICG/cMBP}$ (A), $\text{Fe}_3\text{O}_4@\text{mSiO}_2$ (B), and $\text{Fe}_3\text{O}_4@\text{mSiO}_2\text{-ICG/cMBP}$ (C). Size variations of $\text{mSiO}_2\text{-ICG/cMBP}$ (D), $\text{Fe}_3\text{O}_4@\text{mSiO}_2$ (E), and $\text{Fe}_3\text{O}_4@\text{mSiO}_2\text{-ICG/cMBP}$ (F) dispersed in 0.9 % NaCl, PBS, and cell medium. (G) Hemolysis rate of $\text{mSiO}_2\text{-ICG/cMBP}$, $\text{Fe}_3\text{O}_4@\text{mSiO}_2$, and $\text{Fe}_3\text{O}_4@\text{mSiO}_2\text{-ICG/cMBP}$. (H) Binding activity of $\text{Fe}_3\text{O}_4@\text{mSiO}_2\text{-FITC/cMBP}$ or $\text{Fe}_3\text{O}_4@\text{mSiO}_2\text{-FITC/cMBP+HGF}$ to c-Met at various concentrations.

et al., 2021). When $\text{Fe}_3\text{O}_4@\text{mSiO}_2\text{-FITC}/\text{cMBP}$ and HGF was introduced to the c-Met coated microplate, our nanoprobe inhibited the affinity of c-Met to HGF (Fig. 3H). Altogether, cMBP might contribute to strong binding affinity between nanoprobe and overexpressed c-Met in TNBC cells.

3.3. Cell viability and cellular internalization *in vitro*

It has been confirmed that metastatic squamous cell carcinoma (SCC) cells overexpress c-Met protein (Ozawa, et al., 2015). In the constructed murine SCC model, the high levels of angiogenesis factors and on tumorigenesis and metastasis enhancement were accompanied by

with HGF/c-Met pathway (Raj, et al., 2022). Based on this, cell viabilities and cellular internalization of cMBP-conjugated nanoprobe at different doses were studied against MDA-MB 231 (TNBC cell line) and SCC7 cells. As shown in Fig. 4A,B,D,E, even the incubated concentration set as high as 800 $\mu\text{g}/\text{mL}$ and the co-culture time extended as long as 24 hr, the cell viabilities of both two kinds of tumor cells still remained over 90%, pronouncedly confirming that the $\text{Fe}_3\text{O}_4@\text{mSiO}_2\text{-cMBP}$ nanocomposites possessed perfect biocompatibility. In addition, negligible cell toxicity was discovered in normal macrophage (Raw 264.7) when the concentration of $\text{Fe}_3\text{O}_4@\text{mSiO}_2\text{-ICG}/\text{cMBP}$ increased to 600 $\mu\text{g}/\text{mL}$ (Fig. S8), pronouncedly reflecting the exceptional biocompatibility *in vitro*. Further, owing to c-Met receptor is known to be overexpressed in these

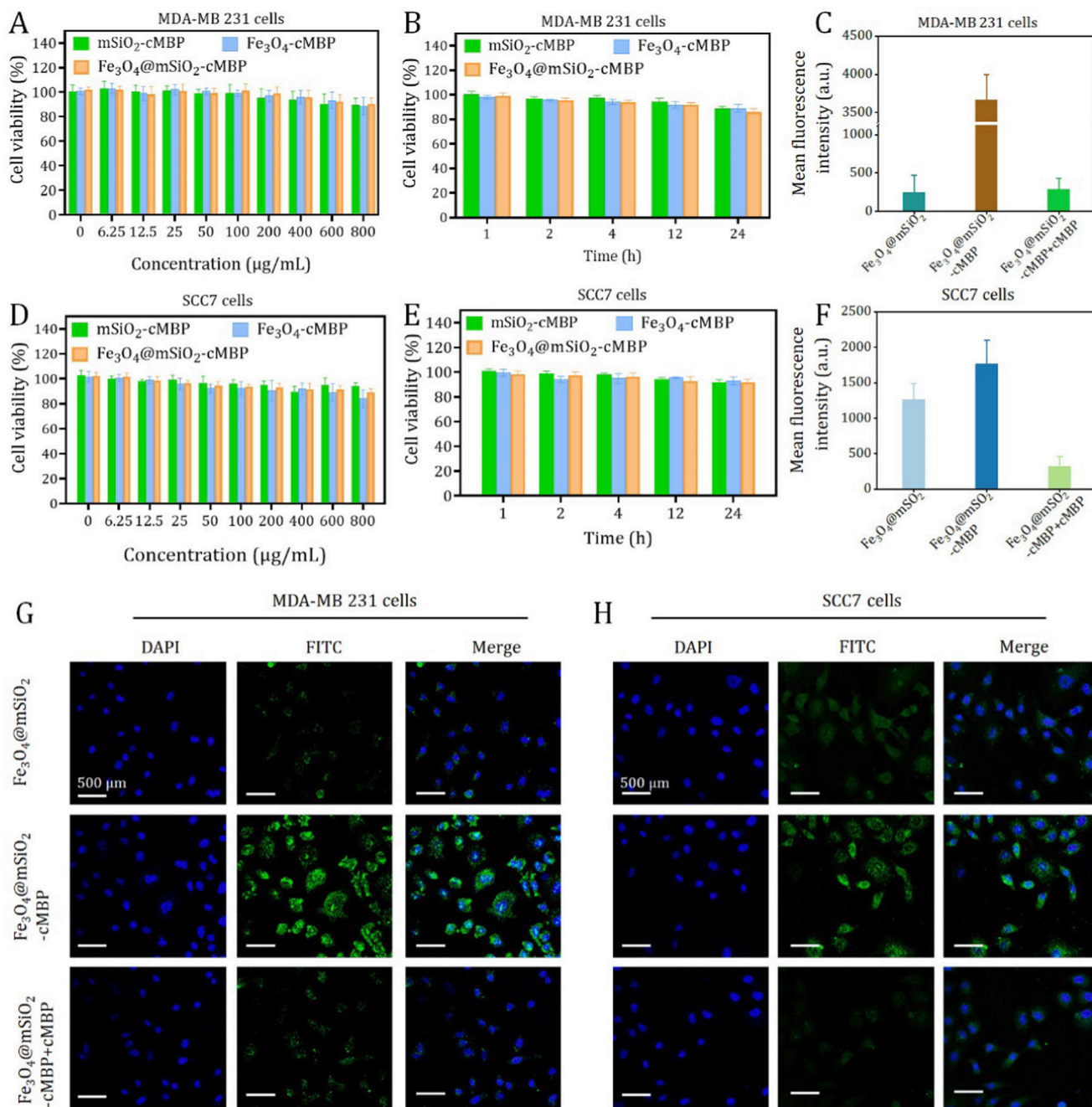


Fig. 4. Cell viability of MDA-MB 231 cells after treated with mSiO₂-cMBP, Fe₃O₄-cMBP and Fe₃O₄@mSiO₂-cMBP at different concentrations (A) or various incubation periods (B). Cell viability of SCC7 cells after treated with mSiO₂-cMBP, Fe₃O₄-cMBP and Fe₃O₄@mSiO₂-cMBP at different concentrations (D) or various incubation periods (E). Quantitative fluorescence intensity (C) and CLSM images (G) of Fe₃O₄@mSiO₂, Fe₃O₄@mSiO₂-cMBP and Fe₃O₄@mSiO₂-cMBP+cMBP treated MDA-MB 231 cells. Quantitative fluorescence intensity (F) and CLSM images (H) of Fe₃O₄@mSiO₂, Fe₃O₄@mSiO₂-cMBP and Fe₃O₄@mSiO₂-cMBP+cMBP treated SCC7 cells.

two carcinoma cells, thus, cMBP-conjugated $\text{Fe}_3\text{O}_4@\text{mSiO}_2$ (labeled with FITC) was expected to be effectively targeted the cancerous cells. Fig. 4G, C shows the CLSM images and quantitative fluorescence intensities of MDA-MB 231 cells after incubated with $\text{Fe}_3\text{O}_4@\text{mSiO}_2$ and $\text{Fe}_3\text{O}_4@\text{mSiO}_2\text{-cMBP}$ for 6 hr, respectively. These two nanocomposites appeared as green light and the cMBP anchored group had much stronger luminescence intensity than the exposed surface of $\text{Fe}_3\text{O}_4@\text{mSiO}_2$ nanocomposites, indicating that c-Met receptor-mediated tumor cell recognition accelerated the cellular internalization of $\text{Fe}_3\text{O}_4@\text{mSiO}_2\text{-cMBP}$. Whereas, in the MDA-MB 231 cells pretreated with cMBP groups for blocking c-Met, the green fluorescence had decreased twelve folds (Fig. 4C). We also conducted cellular endocytosis of ICG loaded nanoprobes (Ex 633 nm, Em, 750 nm) toward MDA-MB 231 by CLSM, as shown in Fig. S9, in comparison with other two groups, prominent high red fluorescence from ICG can be detected in $\text{Fe}_3\text{O}_4@\text{mSiO}_2\text{-ICG/cMBP}$. In addition, similar fluorescent trend was found in SCC7 groups, while in sharp contrast, $\text{Fe}_3\text{O}_4@\text{mSiO}_2\text{-cMBP}$ treated TNBC cell showed relative two times cellular endocytosis than that of SCC7 cell (Fig. S10). The underlying mechanism of stronger green fluorescence in 4 T1 cells might be attributed to relatively higher c-Met expression in 4 T1 cells (Fig. S11). All above findings demonstrated the more effective diagnostic ability of cMBP-conjugated nanoagents toward TNBC tumors.

3.4. NIR II fluorescence imaging and MRI properties in vitro and in vivo

In vitro NIR II luminescent bioimaging capacity was evaluated by a home-made NIR II fluorescence imaging system for small animal. In accordance with ICG, the strong off-peak emission (beyond 1000 nm) of $\text{Fe}_3\text{O}_4@\text{mSiO}_2\text{-ICG/cMBP}$ was appraised (Fig. S12). Expectedly, with the increase of dosage, the NIR II luminescence intensity of $\text{Fe}_3\text{O}_4@\text{mSiO}_2\text{-ICG/cMBP}$ were increasingly brighter under 808-nm continuous laser illumination ($P=0.5\text{ W/cm}^2$, 100 ms, 1000 nm long-pass filter) (Fig. 5A). A highly linear correlation with ($R^2 = 0.999$) of mean fluorescence intensity at a range of dose from 0.345 to 4.189 $\mu\text{g/mL}$ (Fig. 5B). Besides, T1-weighted MRI pictures of the fabricated $\text{Fe}_3\text{O}_4@\text{mSiO}_2\text{-ICG/cMBP}$ nanocomposite were obtained by using a MR scanner (3.0 T). As displayed in Fig. 5C, the novel Fe_3O_4 based nanocomposite presented an apparent Fe concentration-dependent

brightening effect, profoundly demonstrating the sensitive T1 weighted contrast effects. Additionally, Fig. 5D clearly illustrates the excellent linear relationship ($R^2 = 0.999$). The *in vitro* NIR II/MRI results suggested that the $\text{Fe}_3\text{O}_4@\text{mSiO}_2\text{-ICG/cMBP}$ nanocomposite had the huge potential to be applied as a contrast agent for sensitive fluorescence imaging and MRI in malignant tumor discrimination.

Aforementioned excellent fluorescence feature of $\text{Fe}_3\text{O}_4@\text{mSiO}_2\text{-ICG/cMBP}$ inspired us to evaluate the corresponding *in vivo* NIR II fluorescence imaging effect on the TBNC lymphatic metastasis bearing nude mice. To better address the precise recognition of our nanoprobe (with cMBP) toward TNBC tumor tissues, we selected $\text{Fe}_3\text{O}_4@\text{mSiO}_2\text{-ICG}$ (without cMBP) as the control agent. After caudal-vein administration of these two nanocomposites for 15 min, bioimaging was executed as depicted in Fig. 6A. Apparently, NIR II fluorescent signals in the lymphatic TNBC metastasis could be gradually observed in both “with” and “without” groups at 1 h post-administration. Evidently, mice in the latter group only presented feeble signal, expectedly, stronger fluorescence was visualized in cMBP conjugated group, especially at 3 h, when the total contour of the small lesion can be successfully distinguished. Then, in the TNBC metastasis tissues of the two groups, NIR II light decayed from this timepoint. Concurrently, $\text{Fe}_3\text{O}_4@\text{mSiO}_2\text{-ICG/cMBP}$ produced relatively higher signal to background ratios (SBR) when compared to $\text{Fe}_3\text{O}_4@\text{mSiO}_2\text{-ICG}$ at every time period, particularly, an optimal SBR value was obtained in the “with” group at 3 h (13.6 ± 1.5 vs. 5.9 ± 1.4) (Fig. 6C). This result was substantially due to more efficacious tumor concentrated effect of $\text{Fe}_3\text{O}_4@\text{mSiO}_2\text{-ICG/cMBP}$. Further, after tail-vein injection of $\text{Fe}_3\text{O}_4@\text{mSiO}_2\text{-ICG/cMBP}$ (15 mg/kg), the vital organs were imaged under NIR II fluorescence imaging system, even massive nanoprobes accumulated in the reticuloendothelial system at 12 hr, they were approximately metabolized at 48 hr (Fig. S13), primarily reflecting the low side effect *in vivo*. To further explore the feasibility of our nanoprobes for MRI, gadopentetic acid (Gd-DTPA), as a clinical MRI contrast agent, was used as the control. After intravenous administration of above two agents, as illustrated in Fig. 6B, metastasis area became strongest in Gd-DTPA treated mice at 2 h post-administration, while almost all T1 weighted signal drastically vanished at 3 h, this performance might be assigned to the low blood retention time of this complex. Excitingly, the MRI signal of the targeted group appeared at 15 min post-administration and achieved at

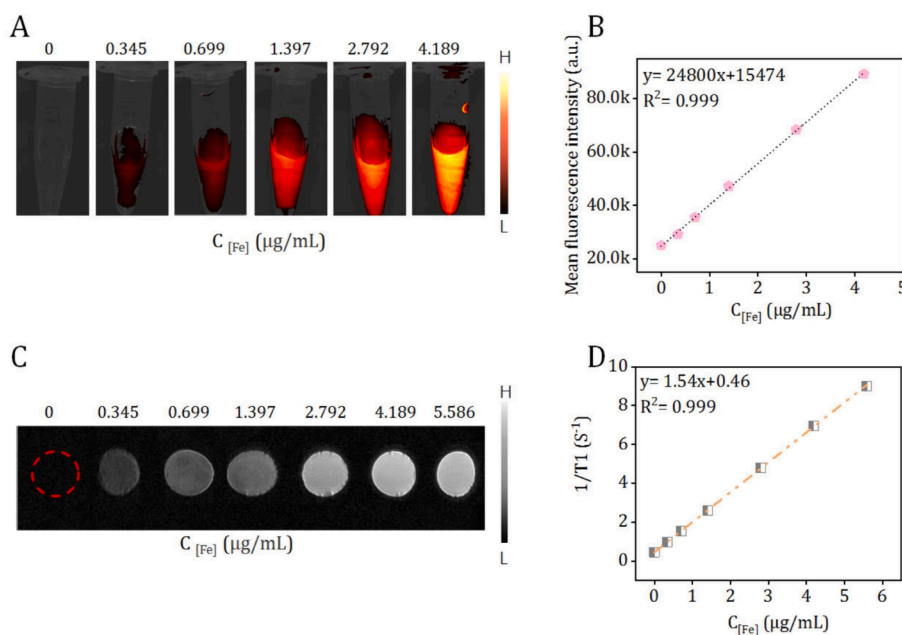


Fig. 5. (A) NIR II fluorescent and (C) MRI bioimages of the fabricated $\text{Fe}_3\text{O}_4@\text{mSiO}_2\text{-ICG/cMBP}$ at various concentrations. Plots of the mean fluorescence intensity (B) and $1/T1$ (S^{-1}) (D) vs. the dosage of $\text{Fe}_3\text{O}_4@\text{mSiO}_2\text{-ICG/cMBP}$.

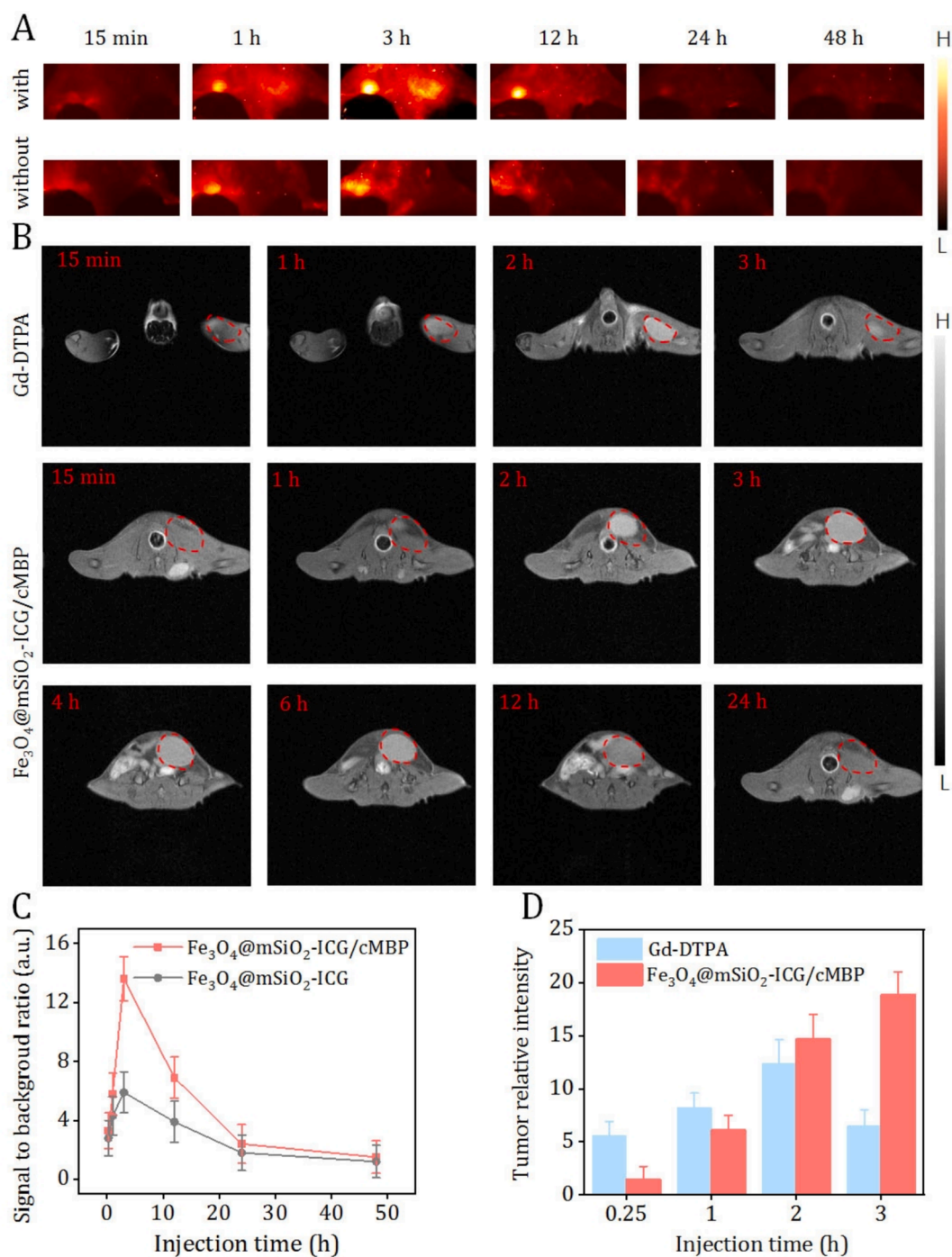


Fig. 6. (A) *In vivo* NIR II fluorescent bioimages of lymphatic metastasis bearing naked mouse after caudal-vein injection of Fe_3O_4 @mSiO₂-ICG (without) or Fe_3O_4 @mSiO₂-ICG/cMBP (with) at different time periods. (B) MRI bioimages of lymphatic metastasis bearing naked mouse after intravenous administration of Gd-DTPA and Fe_3O_4 @mSiO₂-ICG/cMBP for different times. (C) SBR values of Fe_3O_4 @mSiO₂-ICG (without) or Fe_3O_4 @mSiO₂-ICG/cMBP (with) at different time periods. (D) Relative MRI signal intensities of Gd-DTPA and Fe_3O_4 @mSiO₂-ICG/cMBP at 15 min, 1 hr, 2 hr and 3 hr.

the maximum level at 3 h, then it slowly started to decrease along with time extension. The highest tumor enrichment time point was coincident with fluorescence imaging. In the meantime, compared with Gd-DTPA, Fe_3O_4 @mSiO₂-ICG/cMBP still maintained a significantly higher intensity even after 6 h post-administration. Even the relative signal intensity of targeted group was slightly less than Gd-DTPA group (12.4 vs. 14.7) at 2 h post injection, inspiringly, it intensely increased to three times higher than that of Gd-DTPA (Fig. 6D). This feature can be attributed to PEG coatings on Fe_3O_4 @mSiO₂-ICG/cMBP. It shielded nanoprobes from aggregation, phagocytosis as well as prolonging

systemic blood circulation time (Suk, et al., 2016). All above data illustrated that the robust, specific binding affinity of cMBP-grafted nanoprobes toward c-Met overexpressed TNBC carcinoma and it can be exploited as an effective contrast nanoagent for MRI/NIR II fluorescence imaging.

3.5. Biocompatibility assessment *in vivo*

Additionally, *in vivo* biocompatibility of Fe_3O_4 @mSiO₂-ICG/cMBP was determined. After intravenous administrated our nanoprobes for 7

days and 30 days, blood samples and major organ tissue were collected. Blood bio-chemical tests and H&E staining studies were conducted for exploring the biosafety of $\text{Fe}_3\text{O}_4@\text{mSiO}_2\text{-ICG/cMBP}$ *in vivo*. Here, the serum bio-chemistry factors include alanine transaminase (ALT, Fig. 7A), alkaline phosphatase (ALP, Fig. 7B), aspartate transaminase (AST, Fig. 7C), total bilirubin (TBIL, Fig. 7D), serum creatinine (CRE, Fig. 7E), blood urea nitrogen (BUN, Fig. 7F) and creatine kinase (CK, Fig. 7G). Collectively, in comparison with control group (PBS treatment), there were insignificant discrepancy in the seven indexes of the $\text{Fe}_3\text{O}_4@\text{mSiO}_2$ based groups at 7 days and 30 days post-administration. In the bargain, both scale-down and full-size H&E-stained-images of the main normal organ tissues (including heart, liver, spleen, lung and kidney) revealed no apparent pathological injury or normal cellular damage were discovered (Fig. 7H, S14), preliminarily illustrating the excellent *in vivo* histocompatibility of $\text{Fe}_3\text{O}_4@\text{mSiO}_2\text{-ICG/cMBP}$ as well as its potent bio-application for TNBC patients.

4. Conclusion

In this research, a TNBC targeted nanocomposite with NIR II fluorescence and MRI (T1) imaging abilities has been successfully designed and synthesized for the precisely distinguishing the lymphatic metastasis. Our findings suggested that $\text{Fe}_3\text{O}_4@\text{mSiO}_2\text{-ICG/cMBP}$ nanoprobes can induce efficacious cellular recognition and enhance the followed

endocytosis toward highly overexpressed c-Met cell lines with low cytotoxicity. Significantly, the whole lymphatic TNBC metastasis contour *in vivo* was accurately imaged by NIR II luminescent imaging with higher SBR and MRI with remarkably higher T1 weighted signal intensity than Gd-DTPA that highlighted our work. No obvious off-targeted damage was found even after one month of tail-vein administration of nanocomposite, verifying that it can be served as an attractive contrast agent for multi-modal molecular imaging.

Funding

1. National Natural Science Foundation of China (Grant No: 82172051) – Recipient: Ying Yuan
2. National Natural Science Foundation of China (Grant No: 82172049) – Recipient: Xiaofeng Tao
3. Medical-Engineering Cross-Research Fund (Grant No: YG2022QN056) – Recipient: Weiqing Tang
4. Fundamental research program funding of Ninth People's Hospital affiliated to Shanghai Jiao Tong University School of Medicine (Grant No: JYZZ185) – Recipient: Jingbo Wang

Declaration of competing interest

The authors declare that they have no known competing financial

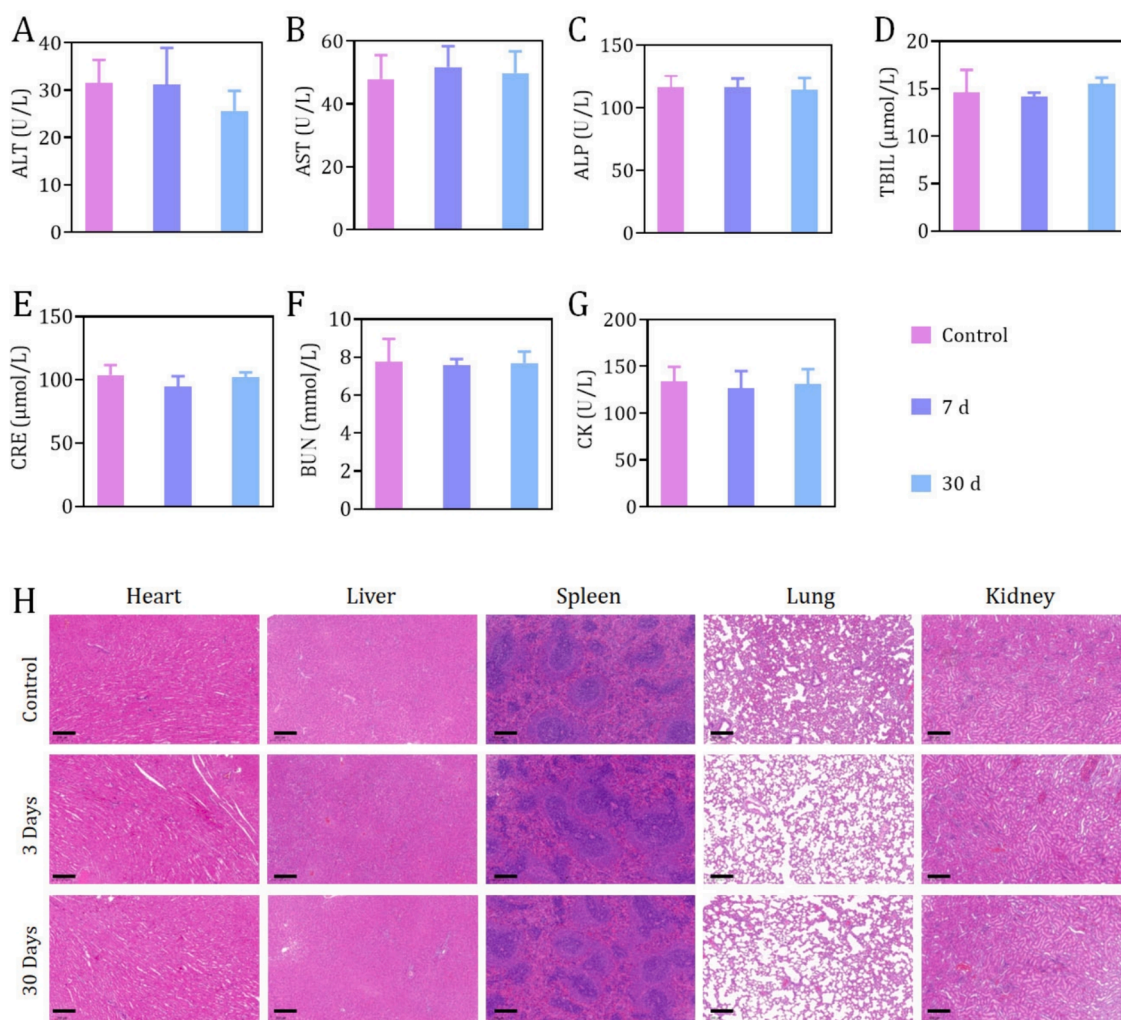


Fig. 7. Serum bio-chemistry studies, including factors like ALT (A), ALP (B), AST (C), TBIL (D), CRE (E), BUN (F), CK (G) of healthy mice after 7 days or 30 days post-administration of $\text{Fe}_3\text{O}_4@\text{mSiO}_2\text{-ICG/cMBP}$. (H) H&E-stained-images of the main organs tissues (including heart, liver, spleen, lungs, kidney) resected from mice after 7 days, 30 days treatment of $\text{Fe}_3\text{O}_4@\text{mSiO}_2\text{-ICG/cMBP}$. PBS treated mice were set as control.

interests or personal relationships that could have appeared to influence the work reported in this paper.

Acknowledgements

This work was supported by the Medical-Engineering Cross-Research Fund (Grant No: YG2022ON056 and YG2024QNA23).

Appendix A. Supplementary data

Supplementary data to this article can be found online at <https://doi.org/10.1016/j.arabjc.2024.105919>.

References

- Antaris, A.L., Chen, H., Cheng, K., Sun, Y., Hong, G., Qu, C., Diao, S., Deng, Z., Hu, X., Zhang, B., Zhang, X., Yaghi, O.K., Alamparambil, Z.R., Hong, X., Cheng, Z., Dai, H., 2016. A small-molecule dye for NIR-II imaging. *Nat. Mater.* 15, 235–242. <https://doi.org/10.1038/nmat4476>.
- Antaris, A.L., Chen, H., Diao, S., Ma, Z., Zhang, Z., Zhu, S., Wang, J., Lozano, A.X., Fan, Q., Chew, L., Zhu, M., Cheng, K., Hong, X., Dai, H., Cheng, Z., 2017. A high quantum yield molecule-protein complex fluorophore for near-infrared II imaging. *Nat. Commun.* 8, 15269. <https://doi.org/10.1038/ncomms15269>.
- Asleh, K., Riaz, N., Nielsen, T., 2022. Heterogeneity of triple negative breast cancer: Current advances in subtyping and treatment implications. *J. Exp. Clin. Cancer Res.* 41 (1), 265. <https://doi.org/10.1186/s13046-022-02476-1>.
- Bai, J., Qiu, S., Zhang, G., 2023. Molecular and functional imaging in cancer-targeted therapy: current applications and future directions. *Signal Transduct. Tar.* 8, 89. <https://doi.org/10.1038/s41392-023-01366-y>.
- Barick, K.C., Singh, S., Bahadur, D., Lawande, M.A., Patkar, D.P., Hassan, P.A., 2014. Carboxyl decorated Fe₃O₄ nanoparticles for MRI diagnosis and localized hyperthermia. *J. Colloid Interf. Sci.* 418, 120–125. <https://doi.org/10.1016/j.jcis.2013.11.076>.
- Carr, J.A., Franke, D., Caram, J.R., Perkinson, C.F., Saif, M., Askoxyllakis, V., Datta, M., Fukumura, D., Jain, R.K., Bawendi, M.G., Burns, O.T., 2018. Shortwave infrared fluorescence imaging with the clinically approved near-infrared dye indocyanine green. *Proc. Natl. Acad. Sci. USA* 115 (17), 4465–4470. <https://doi.org/10.1073/pnas.1718917115>.
- Charafe-Jauffret, E., Ginestier, C., Monville, F., Finetti, P., Adélaïde, J., Cervera, N., Fekairi, S., Xerri, L., Jacquemier, J., Birnbaum, D., Bertucci, F., 2006. Gene expression profiling of breast cell lines identifies potential new basal markers. *Oncogene* 25 (15), 2273–2284. <https://doi.org/10.1038/sj.onc.1209254>.
- Chu, M., Shao, Y., Peng, J., Dai, X., Li, H., Wu, Q., Shi, D., 2013. Near-infrared laser light mediated cancer therapy by photothermal effect of Fe₃O₄ magnetic nanoparticles. *Biomaterials* 34, 4078–4088. <https://doi.org/10.1016/j.biomaterials.2013.01.086>.
- Corti, C., Nicolò, E., Curigliano, G., 2021. Novel immune targets for the treatment of triple-negative breast cancer. *Expert. Opin. Ther. Targets* 25 (10), 815–834. <https://doi.org/10.1080/14728222.2021.2006187>.
- Deng, Y., Qi, D., Deng, C., Zhang, X., Zhao, D., 2008. Superparamagnetic high-magnetization microspheres with an Fe₃O₄@SiO₂ Core and perpendicularly aligned mesoporous SiO₂ shell for removal of microcystins. *J. Am. Chem. Soc.* 130 (1), 28–29. <https://doi.org/10.1021/ja0777584>.
- Dubravka, N., Marta, J., Jovana, P., Danijela, V., Tatjana, R., Sanja, R.S., Rakocevic, R., Nestic, D., Pantic, I., 2018. Application of iron nanoparticles in contemporary physiology and cell biology research. *Rev. Adv. Meter. Sci.* 53, 74–78. <https://doi.org/10.1515/rams-2018-0005>.
- Fang, Z., Li, X., Xu, Z., Du, F., Wang, W., Shi, R., Gao, D., 2019. Hyaluronic acid-modified mesoporous silica-coated superparamagnetic Fe₃O₄ nanoparticles for targeted drug delivery. *Int. J. Nanomedicine* 14, 5785–5797. <https://doi.org/10.2147/IJN.S213974>.
- Fu, J., Su, X., Li, Z., Deng, L., Liu, X., Feng, X., Peng, J., 2021. HGF/c-MET pathway in cancer: from molecular characterization to clinical evidence. *Oncogene* 40, 4625–4651. <https://doi.org/10.1038/s41388-021-01863-w>.
- Gao, D., Luo, Z., He, Y., Yang, L., Hu, D., Liang, Y., Zheng, H., Liu, X., Sheng, Z., 2023. Low-Dose NIR-II Preclinical Bioimaging Using Liposome-Encapsulated Cyanine Dyes. *Small* 19 (17), 2206544. <https://doi.org/10.1002/sml.202206544>.
- Gonçalves, A., Charafe-Jauffret, E., Bertucci, F., Audebert, S., Toiron, Y., Esterni, B., Monville, F., Tarpin, C., Jacquemier, J., Houvenaeghel, G., Chabannon, C., Extra, J. M., Viens, P., Borg, J.P., Birnbaum, D., 2008. Protein profiling of human breast cancer cells identifies novel biomarkers associated with molecular subtypes. *Mol. Cell Proteomics* 7 (8), 1420–1433. <https://doi.org/10.1074/mcp.M700487-MCP200>.
- He, S.Q., Song, J., Qu, J.L., Cheng, Z., 2018. Crucial breakthrough of second near-infrared biological window fluorophores: design and synthesis toward multimodal imaging and theranostics. *Chem. Soc. Rev.* 47 (12), 4258–4278. <https://doi.org/10.1039/c8cs00234g>.
- Hochgräfe, F., Zhang, L., O'Toole, S.A., Browne, B.C., Pinese, M., Cubas, A.P., Lehrbach, G.M., Croucher, D.R., Rickwood, D., Boulghourjian, A., Shearer, R., Nair, R., Swarbrick, A., Faratian, D., Mullen, P., Harrison, D.J., Biankin, A.V., Sutherland, R.L., Raftery, M.J., Daly, R.J., 2010. Tyrosine phosphorylation profiling reveals the signaling network characteristics of basal breast cancer cells. *Cancer Res.* 70 (22), 9391–9401. <https://doi.org/10.1158/0008-5472.CAN-10-0911>.
- Hu, Z., Fang, C., Li, B., Zhang, Z., Cao, C., Cai, M., Su, S., Sun, X., Shi, X., Li, C., Zhou, T., Zhang, Y., Chi, C., He, P., Xia, X., Chen, Y., Gambhir, S.S., Cheng, Z., Tian, J., 2020. First-in-human liver-tumour surgery guided by multispectral fluorescence imaging in the visible and near-infrared-I/II windows. *Nat. Biomed. Eng.* 4 (3), 259–271. <https://doi.org/10.1038/s41551-019-0494-0>.
- Ibrahim, A.H., Smatt, J.H., Govardhanam, N.P., Ibrahim, H.M., Ismael, H.R., Afoua, M. I., Samy, A.M., Rosenholm, J.M., 2020. Formulation and optimization of drug-loaded mesoporous silica nanoparticle-based tablets to improve the dissolution rate of the poorly water-soluble drug silymarin. *Eur. J. Pharm. Sci.* 142, 105103. <https://doi.org/10.1016/j.ejps.2019.105103>.
- Jayaraman, S., Rajarathinam, T., Jang, H.G., Thirumalai, D., Lee, J., Paik, H.J., Chang, S. C., 2023. Ruthenium-anchored carbon sphere-customized sensor for the selective amperometric detection of melatonin. *Biosensors* 13 (10), 936. <https://doi.org/10.3390/bios13100936>.
- Lee, J., Gordon, A.C., Kim, H., Park, W., Cho, S., Lee, B., Larson, A.C., Rozhkova, E.A., Kim, D.H., 2016. Targeted multimodal nano-reporters and optimization of pre-procedural MRI and intra-operative image-guidance. *Biomaterials* 109, 69–77. <https://doi.org/10.1016/j.biomaterials.2016.09.013>.
- Li, J., Jiang, R.C., Wang, Q., Li, X., Hu, X.M., Yuan, Y., Lu, X.M., Wang, W.J., Huang, W., Fan, Q.L., 2019. Semiconducting polymer nanotheranostics for NIR-II/Photoacoustic imaging-guided photothermal initiated nitric oxide/photothermal therapy. *Biomaterials* 217, 119304. <https://doi.org/10.1016/j.biomaterials.2019.119304>.
- Li, D., Yang, J., Xu, Z., Li, Y., Sun, Y., Wang, Y., Zou, H., Wang, K., Yang, L., Wu, L., Sun, X., 2023. c-Met-targeting ¹⁹F MRI nanoparticles with ultralong tumor retention for precisely detecting small or ill-defined colorectal liver metastases. *Int. J. Nanomed.* 18, 2181–2196. <https://doi.org/10.2147/IJN.S403190>.
- Liu, P., Wang, T., Yang, Z., Hong, Y., Xie, X., Hou, Y., 2020. Effects of Fe₃O₄ nanoparticle fabrication and surface modification on Chlorella sp. harvesting efficiency. *Sci. Total Environ.* 704, 135286. <https://doi.org/10.1016/j.scitotenv.2019.135286>.
- Lugert, S., Unterwerg, H., Mühlberger, M., Janko, C., Draak, S., Ludwig, F., Eberbeck, D., Alexiou, C., Friedrich, R.P., 2018. Cellular effects of paclitaxel-loaded iron oxide nanoparticles on breast cancer using different 2D and 3D cell culture models. *Int. J. Nanomed.* 14, 161–180. <https://doi.org/10.2147/IJN.S187886>.
- Marra, A., Trapani, D., Viale, G., Criscitiello, C., Curigliano, G., 2020. Practical classification of triple-negative breast cancer: intratumoral heterogeneity, mechanisms of drug resistance, and novel therapies. *npj Breast Cancer* 6, 54. <https://doi.org/10.1038/s41523-020-00197-2>.
- McHugh, K.J., Jing, L., Behrens, A.M., Jayawardena, S., Tang, W., Gao, M., Langer, R., Jaklenc, A., 2018. Biocompatible semiconductor quantum dots as cancer imaging agents. *Adv. Mater.* 30, 1706356. <https://doi.org/10.1002/adma.201706356>.
- Ozawa, Y., Nakamura, Y., Fujishima, F., Felizola, S.J., Takeda, K., Okamoto, H., Ito, K., Ishida, H., Konno, T., Kamei, T., Miyata, G., Ohuchi, N., Sasano, H., 2015. c-Met in esophageal squamous cell carcinoma: an independent prognostic factor and potential therapeutic target. *BMC Cancer* 15, 451. <https://doi.org/10.1186/s12885-015-1450-3>.
- Raj, S., Kesari, K.K., Kumar, A., Rathi, B., Sharma, A., Gupta, P.K., Jha, S.K., Jha, N.K., Slama, P., Roychoudhury, S., Kumar, D., 2022. Molecular mechanism(s) of regulation(s) of c-MET/HGF signaling in head and neck cancer. *Mol. Cancer* 21, 31. <https://doi.org/10.1186/s12943-022-01503-1>.
- Rajarathinam, T., Santha, M.M., Jayaraman, S., Manivasagan, P., Bharathiraja, S., Oh, Y. O., Oh, J., 2019. Synthesis of silica-coated magnetic hydroxyapatite composites for drug delivery applications. *J. Nano. Technol.* 19, 4. <https://doi.org/10.1166/jnn.2019.15399>.
- Rajarathinam, T., Kwon, M., Thirumalai, D., Kim, S., Lee, S., Yoon, J.H., Paik, H.J., Kim, S., Lee, J., Ha, H.K., 2021. Polymer-dispersed reduced graphene oxide nanosheets and Prussian blue modified biosensor for amperometric detection of sarcosine. *Anal. Chim. Acta* 1175, 338749. <https://doi.org/10.1016/j.aca.2021.338749>.
- Rajarathinam, T., Thirumalai, D., Jayaraman, S., Yang, S., Ishigami, A., Yoon, J.H., Paik, H.J., Lee, J., Chang, S.C., 2024. Glutamate oxidase sheets-Prussian blue grafted amperometric biosensor for the real time monitoring of glutamate release from primary cortical neurons. *Int. J. Biol. Macromol.* 245 (Part 2), 127903. <https://doi.org/10.1016/j.ijbiomac.2023.127903>.
- Ren, F., Ding, L., Liu, H., Huang, Q., Zhang, H., Zhang, L., Zeng, J., Sun, Q., Li, Z., Gao, M., 2018. Ultra-small nanocluster mediated synthesis of Nd³⁺-doped core-shell nanocrystals with emission in the second near-infrared window for multimodal imaging of tumor vasculature. *Biomaterials* 175, 30–43. <https://doi.org/10.1016/j.biomaterials.2018.05.021>.
- Siegel, R.L., Miller, K.D., Fuchs, H.E., Jemal, A., 2022. Cancer Statistics. *CA Cancer J. Clin.* 72 (1), 7–33. <https://doi.org/10.3322/caac.21708>.
- Smeden, V.M., Reitsma, J.B., Riley, R.D., Collins, G., Moon, K.G., 2021. Clinical prediction models: diagnosis versus prognosis. *J. Clin. Epidemiol.* 132, 142–145. <https://doi.org/10.1016/j.jclinepi.2021.01.009>.
- Souri, M., Golzaryan, A., Soltani, M., 2024. Charge-switchable nanoparticles to enhance tumor penetration. *Eur. J. Pharm. Biopharm.* 199, 114310. <https://doi.org/10.1016/j.ejpb.2024.114310>.
- Suk, J.S., Xu, Q., Kim, N., Hanes, J., Ensign, L.M., 2016. PEGylation as a strategy for improving nanoparticle-based drug and gene delivery. *Adv. Drug Deliv. Rev.* 99, 28–51. <https://doi.org/10.1016/j.addr.2015.09.012>.
- Sun, P., Zhang, Y., Li, K., Wang, C., Zeng, F., Zhu, J., Wu, Y., Tao, X., 2019. Image-guided surgery of head and neck carcinoma in rabbit models by intra-operatively defining tumor-infiltrated margins and metastatic lymph nodes. *EBioMedicine* 50, 93–102. <https://doi.org/10.1016/j.ebiom.2019.10.055>.
- Takahashi, R., Toh, U., Iwakuma, N., Mishima, M., Fujii, T., Takenaka, M., Koura, K., Seki, N., Kawahara, A., Kage, M., Ogo, E., Shirouzu, K., 2013. Treatment outcome in

- patients with stage III breast cancer treated with neoadjuvant chemotherapy. *Exp. Ther. Med.* 6 (5), 1089–1095. <https://doi.org/10.3892/etm.2013.1289>.
- Terada, M., Miyashita, M., Kumamaru, H., Miyata, H., Tamura, K., Yoshida, M., Ogo, E., Nagahashi, M., Asaga, S., Kojima, Y., Kadoya, T., Aogi, K., Niikura, N., Iijima, K., Hayashi, N., Kubo, M., Yamamoto, Y., Jinno, H., 2022. Surgical treatment trends and identification of primary breast cancers after surgery in occult breast cancer: a study based on the Japanese national clinical database—breast cancer registry. *Breast Cancer* 29, 98–708. <https://doi.org/10.1007/s12282-022-01348-y>.
- Wang, Y., Feng, M., Lin, B., Peng, X., Wang, Z., Lv, R., 2021. MET-targeted NIR II luminescence diagnosis and up-conversion guided photodynamic therapy for triple-negative breast cancer based on a lanthanide nanoprobe. *Nanoscale* 13 (43), 18125–18133. <https://doi.org/10.1039/d1nr05847a>.
- Wang, P., Li, J., Wei, M., Yang, R., Lou, K., Dang, Y., Sun, W., Xue, F., Liu, X., 2022b. Tumor microenvironment triggered signal-to-noise boosting nanoprobe for NIR-II fluorescence imaging guided tumor surgery and NIR-II photothermal therapy. *Biomaterials* 287, 121636. <https://doi.org/10.1016/j.biomaterials.2022.121636>.
- Wang, F., Qi, X., Geng, J., Liu, X., Li, D., Zhang, H., Zhang, P., He, X., Li, B., Li, Z., Yu, R., Yang, X., Wang, G., 2022a. Template-free construction of hollow mesoporous Fe₃O₄ nanospheres as controlled drug delivery with enhanced drug loading capacity. *J. Mol. Liq.* 347, 118000. <https://doi.org/10.1016/j.molliq.2021.118000>.
- Wei, M., Bai, J., Shen, X., Lou, K., Gao, Y., Lv, R., Wang, P., Lou, X., Zhang, G., 2023a. Glutathione-exhausting nanoprobe for NIR-II fluorescence imaging-guided surgery and boosting radiation therapy efficacy via ferroptosis in breast cancer. *ACS Nano* 17 (12), 11345–11361. <https://doi.org/10.1021/acsnano.3c00350>.
- Wei, Z., Wang, T., Hong, M., Zhong, L., Wang, Y., Huang, M., Yang, W., 2023b. H₂O₂-adapted chemodynamic and photothermal treatments of pancreatic carcinoma using biodegradable mesoporous silica grafted Fe₃O₄ nanopatform decorated with au nanozyme. *J. Drug Deliv. Sci. Tec.* 87, 104773. <https://doi.org/10.1016/j.jddst.2023.104773>.
- Wu, Y., Fan, Q., Zeng, F., Zhu, J., Chen, J., Fan, D., Li, X., Duan, W., Guo, Q., Cao, Z., Birly-Saebo, K., Li, C., Tao, X., 2018. Peptide-functionalized nanoinhibitor restrains brain tumor growth by abrogating mesenchymal-epithelial transition factor (MET) signalling. *Nano Lett.* 18, 5488–5498. <https://doi.org/10.1021/acs.nanolett.8b01879>.
- Wu, J., Yuan, Y., Tao, X.F., 2020. Targeted molecular imaging of head and neck squamous cell carcinoma: a window into precision medicine. *Chin. Med. J. Engl.* 133, 1325–1336. <https://doi.org/10.1097/CM9.0000000000000751>.
- Wu, J., Liu, J., Lin, B., Lv, R., Tao, X., 2021. Met-targeted dual-modal MRI/NIR II imaging for specific recognition of head and neck squamous cell carcinoma. *ACS Biomater. Sci. Eng.* 7, 1640–1650. <https://doi.org/10.1021/acsbomaterials.0c01807>.
- Xie, H., Li, Y., Xiu, Y., Yuan, H., Hu, T., Yang, Y., 2023. Biodegradable mesoporous Co₃O₄ based nanocarriers with intrinsic lung carcinoma suppression for NIR II fluorescence bioimaging and photothermal augmented photodynamic therapy. *Mater. Design* 233, 112267. <https://doi.org/10.1016/j.matdes.2023.112267>.
- Xu, H., Stabile, L.P., Gubish, C.T., Gooding, W.E., Grandis, J.R., Siegfried, M., 2011. Dual blockade of EGFR and c-Met abrogates redundant signaling and proliferation in head and neck carcinoma cells. *Clin. Cancer Res.* 17, 4425–4438. <https://doi.org/10.1158/1078-0432.CCR-10-3339>.
- Xu, H.B., Yang, Y., Lu, L.F., Yang, Y.W., Zhang, Z.C., Zhao, C.X., Zhang, F., Fan, Y., 2022. Orthogonal multiplexed NIR-II imaging with excitation-selective lanthanide-based nanoparticles. *Anal. Chem.* 94, 3661–3668. <https://doi.org/10.1021/acs.analchem.1c05253>.
- Yang, Y., Huang, M., Qian, J., Gao, D., Liang, X., 2020. Tunable Fe₃O₄ Nanorods for Enhanced Magnetic Hyperthermia Performance. *Sci. Rep.* 10, 8331. <https://doi.org/10.1038/s41598-020-65095-w>.
- Yang, R., Wang, P., Lou, K., Dang, Y., Tian, H., Li, Y., Gao, Y., Huang, W., Zhang, Y., Liu, X., Zhang, G., 2022. Biodegradable nanoprobe for NIR-II fluorescence image-guided surgery and enhanced breast cancer radiotherapy efficacy. *Adv. Sci.* 9 (12), e2104728.
- Yu, T., Di, G., 2017. Role of tumor microenvironment in triple-negative breast cancer and its prognostic significance. *Chin. J. Cancer Res.* 29 (3), 237–252. <https://doi.org/10.21147/j.issn.1000-9604.2017.03.10>.
- Zhao, H., Zhao, H., Jiao, Y., Zhu, Y., Liu, C., Li, F., Wang, Y., Gu, Z., Yang, D., 2020. Biosynthetic molecular imaging probe for tumor-targeted dual-modal fluorescence/magnetic resonance imaging. *Biomaterials* 256, 120220. <https://doi.org/10.1016/j.biomaterials.2020.120220>.
- Zheng, Z., Jia, Z., Qu, C., Dai, R., Qin, Y., Rong, S., Liu, Y., Cheng, Z., Zhang, R., 2021. Biodegradable Silica-Based Nanotheranostics for Precise MRI/NIR-II Fluorescence Imaging and Self-Reinforcing Antitumor Therapy. *Small* 17 (10), e2006508.